



Three-roller continuous setting round process for longitudinally submerged arc welding pipes

Xue-ying HUANG^{1,2}, Jun ZHAO^{1,2}, Gao-chao YU^{1,2}, Qing-dang MENG^{1,2}, Zhen-kai MU^{1,2}, Rui-xue ZHAI^{1,2}

1. Key Laboratory of Advanced Forging & Stamping Technology and Science, Ministry of Education of China, Yanshan University, Qinhuangdao 066004, China;
2. School of Mechanical Engineering, Yanshan University, Qinhuangdao 066004, China

Received 21 May 2020; accepted 21 December 2020

Abstract: In order to solve the problems of excess ovality and cross-section distortion of longitudinally submerged arc welding pipes after forming, a new three-roller continuous setting round process was proposed. This process can be divided into three stages: loading stage, roll bending stage and unloading stage. Based on the discretization idea, the mechanical model of the primary statically indeterminate problem of the longitudinally submerged arc welding pipes at the roll bending stage was established, and the deformation response was obtained. The simulation and theoretical results show that there are three positive bending regions and three reverse bending regions along the circumference of the pipe. The loading force of each roller shows growth, stability and downward trend with time. The error between the theoretical fitting curve and the simulated data point is very small, and the simulation results verify the reliability of the theoretical calculation. The experimental results show that the residual ovality decreases with the increase of the reduction, and the reduction of the turning point is the optimum reduction. In addition, the residual ovality of the pipe is less than 0.7% without cross-section distortion, which verifies the feasibility of this process.

Key words: longitudinally submerged arc welding pipes; three-roller continuous setting round; statically indeterminate problem; mechanical model; ovality; optimum reduction

1 Introduction

The longitudinally submerged arc welding (LSAW) pipe is a typical large thin-walled pipe and is used in various industrial fields. Similarly, thin-walled pipes are also essential lightweight components in the aerospace industry. Scholars have done more and more extensive researches on thin-walled pipes. JUNIOR et al [1] studied a failure analysis of elastic-plastic thin-walled pipes under a combination of internal pressure and axial load (monotonic or alternating). HOSSEINI et al [2] evaluated an energy absorption capacity of the A15083 thin-walled tube and also studied the microstructure, mechanical properties, and

anisotropy coefficients in the peripheral and axial directions. CHEGENI et al [3] used experimental and numerical methods to study the influence of corrosion depth and corrosion shape on the performance of corroded thin-wall steel pipes under the combined action of internal pressure and four-point bending load. ZHAO et al [4] proposed a more direct assessment for welded clad pipes based on a modified reference strain method, and by using the strain-controlled boundary condition, various pipe and weld geometrical shapes were considered in the analysis matrix. BAYKASOĞLU et al [5] researched optimum design of square thin-walled pipe with novel lattice structure under axial impact loading by using a compromise programming based on the multi-objective crash worthiness

optimization procedure. HUANG and ZHANG [6] studied an indentation mode of thin-walled pipes under the three-point bending condition, established a theoretical model for the stress response of thin-walled pipes, and verified the correctness of the theoretical prediction through experiments and simulation. JIANG et al [7] analyzed a numerical control rotating-drawing bending method for thin-walled pipe with a large diameter to thickness ratio, which was of great significance to enrich the bending forming process of large diameter-to-thickness ratio thin-walled (LDTRTW) pipe. TAO et al [8] proposed a modified Johnson–Cook (JC) model by conducting uniaxial tensile tests on large diameter thin-walled (LDTW) Ti–6Al–4V tubes and this model had high prediction accuracy. YU et al [9] studied an elastic–plastic secondary indeterminate problem of thin-walled pipe and verified the reliability of theoretical calculation through numerical simulation. LI et al [10] proposed and realized a sequential multi-objective optimization of LDTW Al-alloy tube bending under uncertainties and verified it by the experimental design and the finite element method.

With the increasing demand for LSAW pipes in various fields, more stringent requirements have been put forward for the quality and performance of pipes. Ovality is one of the important standards for evaluating the quality of pipes. However, due to the heterogeneous stress distribution of pipes, the ovality will increase and cross-section distortion will occur during the process of transportation and long-term placement, so pipes have to be set round. ZHAO et al [11,12] analyzed a process of expansion and setting round and gave the relationship between residual ovality and expanding amount. Based on the basic assumptions of pure bending with small deformation, ZHAO et al [13] theoretically proved an equivalence between curved beams over-bending straightening and straight beams pure bending. It laid a theoretical and experimental foundation for the process of over bending straightening. ZHAN et al [14,15] established a pipe-end ovality intelligent measurement system, and they also set up an intelligent over-bending setting round control system. YU et al [16] proposed a reciprocating bending uniform curvature theorem and verified it experimentally. At the same time, YU et al [17–19] presented a three-roller setting round process and

carried out theoretical analysis and experimental research on the process. HUANG et al [20] carried out simulation and experiments on the three-roller external setting round process for thin-walled pipes, compared the experimental results with the simulation results, and found that the residual ovality was less than 0.2%.

As for the solution of statically indeterminate problems and the comparison of various solution methods, scholars [21–25] have made a detailed research and verified it through simulation and experiments. CAO and DING [21] studied a statically indeterminate problem of 3R2T parallel mechanisms, and the correctness of the theoretical results was verified by the finite element model. NAYAK and SAHA [22] investigated a growth law of the elastic leading edge in the elastic state of ultra-static non-uniform rod. They also realized the solution algorithm by using MATLAB computational simulation software and verified the formula for some simplified problems. GHUKU and SAHA [23] put forward a semi-analytical method for the solution of a statically indeterminate non-uniform bar problem and realized the solution algorithm by utilizing MATLAB computational simulation software. TAN et al [24] presented a method for analysis of statically indeterminate trusses under mechanical-thermal-assembly loadings. The method not only overcame the traditional geometric method to solve the defects of compatible equations, but also had the advantages of simple process, good generality and so on. LÓPEZ et al [25] designed an innovative test system to develop shear failure before and after yielding of the flexural reinforcement in both statically determinate and indeterminate structures.

Based on the characteristics of three-roller setting round and LSAW pipes, a new method of setting round is put forward, namely, three-roller continuous setting round process. In the process, three rollers are placed outside the pipe. By controlling the reduction and rotating speed of the three rollers and the feeding speed of the push plate, the forward and rotary movement of the pipe is realized. This process can be divided into three stages: loading stage, roll bending stage and unloading stage. Based on the discretization idea, the mechanical model of the primary statically indeterminate problem of the pipe in the roll bending stage is established, and the deformation

response is obtained. Through numerical simulation, the theoretical model is verified, and the deformation behavior of the setting round process is described. The influence of this process parameters on the residual ovality is studied by experiments. Additionally, this process is especially suitable for setting round of thin-walled pipes with large length to diameter ratio and small thickness to diameter ratio.

2 Three-roller continuous setting round process

As shown in Fig. 1, the process can be divided into three stages on average: loading stage, roll bending stage and unloading stage. The three stages are evenly distributed in the whole setting round process.

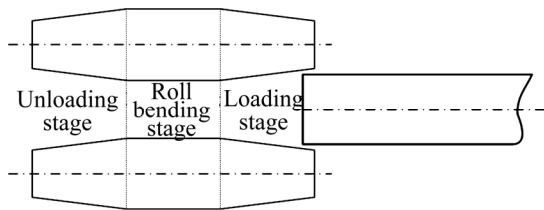


Fig. 1 Three-roller continuous setting round process

Three identical rollers are placed symmetrically in space and the pipe is placed among the three rollers. The actuating motor drives the two lower rollers to rotate synchronously and uniformly, so that the pipe rotates under the friction of two lower rollers. Then the upper roller also starts to rotate under the action of pipe friction, at the same time, the push plate drives the pipe moving forward to achieve the whole movement process. During the process of setting round, each micro-section of the pipe alternately experiences three positive bending regions and three reverse bending regions, that is, the reverse bending regions in contact with each roller and the positive bending regions between adjacent rollers. Moreover, both ends of each roller are provided with a taper. The taper of the loading end ensures that the pipe is smoothly bitten among the three rollers under the push of the push plate. The taper of the unloading end is to make sure that the pipe is smoothly unloaded after experiencing multiple reciprocating bending, so that the curvature of the pipe is unified. The roll bending stage is a straight section to ensure that the pipe produces elastic–plastic deformation at

this stage.

The rollers tapers of the loading end and the unloading end are as follows, respectively:

$$\alpha_j = \frac{3(2H_{\max} + 2a_1 - D_p)}{L_g} \quad (1)$$

$$\alpha_x = \frac{6H_{\max}}{L_g} \quad (2)$$

where α_j is the roller taper of the loading end (rad); α_x is the roller taper of the unloading end (rad); H_{\max} is the maximum reduction allowed for the pipe setting round (mm); a_1 is the long axis radius of the pipe (mm); D_p is the outer diameter of the pipe (mm); L_g is the length of the roller (mm).

As shown in Fig. 2, each roller loads the same distance toward the center of the pipe, and each roller stroke is the reduction, which is recorded as

$$H = R_1 + R - H_j \quad (3)$$

where H is the reduction (mm); R_1 is the radius of the roller (mm); R is the radius of the pipe (mm); H_j is the distance between the center of the roller and the center of the pipe after loading (mm).

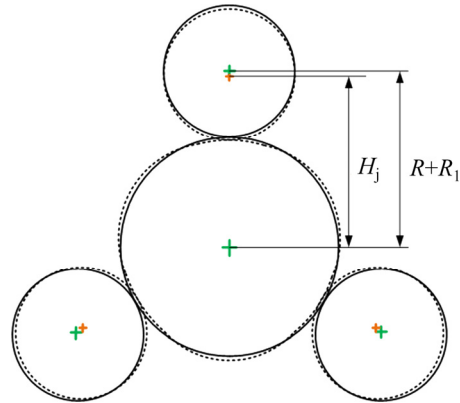


Fig. 2 Loading parameter diagram

3 Theoretical analysis

In the whole continuous setting round process, the maximum bending curvature, minimum bending curvature and maximum loading force all are generated at the roll bending stage. Therefore, the theoretical analysis in this work mainly focuses on the roll bending stage, as shown in Fig. 3.

3.1 Static analysis

According to the deformation characteristics of the roll bending stage, ignoring the influence of

inertial force, the static analysis is performed at the roll bending stage. Since the three-roller continuous setting round process is a small deformation problem, according to the symmetry of the bending deformation of LSAW pipes at the roll bending stage, one-third thin-walled circular pipe is selected as the research object. The mechanical model of the roll bending stage is illustrated in Fig. 4.

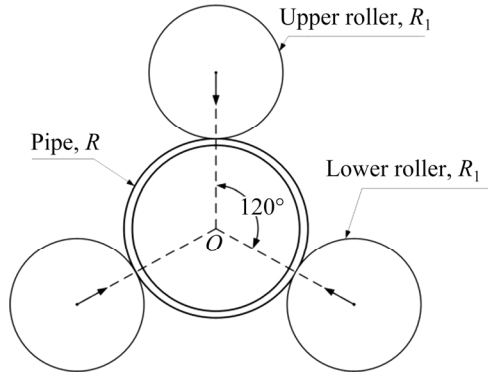


Fig. 3 Schematic diagram showing roll bending stage of three-roller continuous setting round process

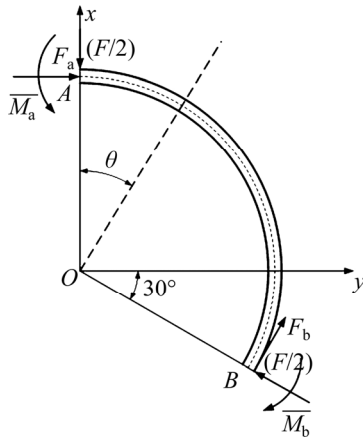


Fig. 4 Mechanical model of one-third circular pipe

According to the static equilibrium equation, the following can be obtained as

$$\sum x=0, F_a+F_b \cos 60^\circ=(F/2) \cos 30^\circ \quad (4)$$

$$\sum y=0, F_b \sin 60^\circ+(F/2) \cos 60^\circ=F/2 \quad (5)$$

Thus,

$$F_a=F_b=\frac{\sqrt{3}}{6} F \quad (6)$$

where F is the loading force of roller (N); F_a is the horizontal cross-section force at position A (N); F_b is the horizontal cross-section force at position B (N).

According to Eqs. (4)–(6), the outer bending

moment of arbitrary micro-section of the pipe-wall can be obtained as

$$\bar{M}_\theta=\bar{M}_a+\frac{F}{2} R \sin \theta-\frac{\sqrt{3}}{6} F R(1-\cos \theta), 0 \leq \theta \leq 2 / 3 \pi \quad (7)$$

where θ is the angle between arbitrary micro-section of the pipe-wall and the axis y (rad); \bar{M}_θ is the outer bending moment with an angle of θ from the axis y (N·mm); \bar{M}_a is the outer bending moment of the upper cross-section (N·mm); R is the geometric neutral layer radius of the circular pipe (mm).

3.2 Elastic–plastic analysis

3.2.1 Basic assumptions

(1) Pure bending assumption: Because the bending process is a small deformation process, it is considered to conform the pure bending deformation characteristics.

(2) Neutral layer coinciding assumption: The strain neutral layer, stress neutral layer and geometric neutral layer always coincide during the deforming process.

(3) Bilinear hardening material model assumption: Effects of initial strain and change of material properties are neglected.

(4) Plane section assumption: Arbitrary plane section remains plane after deforming and no aberrance occurs.

(5) Uniaxial stress state assumption: Any particle on the pipe is uniaxially stretched or compressed during the deforming process.

According to the basic assumption (3), the relationship between strain (ε) and stress (σ) is

$$\sigma=\left\{\begin{array}{l} D \varepsilon+\sigma_0, \varepsilon>\frac{\sigma_s}{E} \\ E \varepsilon, -\frac{\sigma_s}{E} \leq \varepsilon \leq \frac{\sigma_s}{E} \\ D \varepsilon-\sigma_0, \varepsilon<-\frac{\sigma_s}{E} \end{array}\right. \quad (8)$$

$$\sigma_0=\left(1-\frac{D}{E}\right) \sigma_s \quad (9)$$

where σ_s is the yield stress (MPa); E is the elastic modulus (GPa); D is the plastic modulus (MPa).

According to the basic assumption (4), the strain distribution on the pipe-wall micro-section is linear:

$$\varepsilon = Kw - K_0w \tag{10}$$

where K_0 is the initial curvature of the geometric neutral layer (mm^{-1}), $K_0=1/R$; K is the curvature of the geometric neutral layer after loading (mm^{-1}); w is the distance from any particle on the pipe-wall to the geometric neutral layer (mm).

3.2.2 Relationship between bending curvature and inner bending moment

According to the basic assumption (4), the maximum strain on the pipe-wall cross-section occurs on the outer surface:

$$\varepsilon_{\max} = \frac{t}{2}(K - K_0) \tag{11}$$

where t is the thickness of pipe-wall.

As can be seen from the basic assumption (3),

when $|\varepsilon_{\max}| \leq \frac{\sigma_s}{E}$, the cross-section of the curved beam is in an elastic state, so the elastic limitation bending curvature of the positive and reverse bending can be expressed as

$$K_{\text{plim}}^e = K_0 + \frac{2\sigma_s}{tE} \tag{12}$$

$$K_{\text{Rlim}}^e = K_0 - \frac{2\sigma_s}{tE} \tag{13}$$

where K_{plim}^e is the elastic limitation curvature of positive bending (mm^{-1}); K_{Rlim}^e is the elastic limitation curvature of reverse bending (mm^{-1}).

According to the basic assumptions (2)–(5), the relationship between inner bending moment and bending curvature can be obtained:

$$M_\theta = \int \sigma w dA = \begin{cases} DI(K_\theta - K_0) + \frac{B\sigma_0 t^2}{4} - \frac{B\sigma_0 w_s^2}{3}, & K_\theta > K_{\text{plim}}^e \\ EI(K_\theta - K_0), & K_{\text{Rlim}}^e \leq K_\theta \leq K_{\text{plim}}^e \\ DI(K_\theta - K_0) - \frac{B\sigma_0 t^2}{4} + \frac{B\sigma_0 w_s^2}{3}, & K_\theta < K_{\text{Rlim}}^e \end{cases} \tag{14}$$

$$w_s = \frac{\sigma_s}{E(K - K_0)} \tag{15}$$

where M_θ is the inner bending moment (N·mm); K_θ is the bending curvature (mm^{-1}); B is the width (mm); I is the elastic moment of inertia (mm^4); w_s is the height from the elastic-plastic demarcation point to the geometric neutral layer (mm).

According to the Cardano formula and Shengjin formula, the roots of Eq. (14) is determined, so K_θ can be expressed as (the derivation is shown in appendix)

$$K_\theta = \begin{cases} \left. \begin{aligned} & \sqrt[3]{-\frac{q}{2} + \sqrt{\left(\frac{q}{2}\right)^2 + \left(\frac{p}{3}\right)^3}} + \\ & \sqrt[3]{-\frac{q}{2} - \sqrt{\left(\frac{q}{2}\right)^2 + \left(\frac{p}{3}\right)^3}} - \frac{a}{3} + K_0, \Delta \geq 0 \end{aligned} \right\} M_\theta > \frac{Bt^2\sigma_s}{6} \\ \frac{2 \cos\left(\frac{\xi - \pi}{3}\right) \sqrt{m}}{3} - \frac{a}{3} + K_0, \Delta < 0 \\ \left. \begin{aligned} & \frac{M_\theta}{EI} + K_0, -\frac{Bt^2\sigma_s}{6} \leq M_\theta \leq \frac{Bt^2\sigma_s}{6} \\ & \sqrt[3]{-\frac{q_1}{2} + \sqrt{\left(\frac{q_1}{2}\right)^2 + \left(\frac{p_1}{3}\right)^3}} + \\ & \sqrt[3]{-\frac{q_1}{2} - \sqrt{\left(\frac{q_1}{2}\right)^2 + \left(\frac{p_1}{3}\right)^3}} - \frac{a_1}{3} + K_0, \Delta_1 \geq 0 \end{aligned} \right\} M_\theta < -\frac{Bt^2\sigma_s}{6} \\ \frac{2 \cos\left(\frac{\xi_1 - \pi}{3}\right) \sqrt{m_1}}{3} - \frac{a_1}{3} + K_0, \Delta_1 < 0 \end{cases} \tag{16}$$

where

$$a = -\left(\frac{M_\theta}{DI} + \frac{(D-E)Bt^2\sigma_s}{4IDE}\right); c = \frac{(D-E)B\sigma_s^3}{3IDE^3};$$

$$p = -\frac{a^2}{3}; q = \frac{2a^3}{27} + c;$$

$$m = -3p \ (m > 0); n = -9q; \xi = \arccos T;$$

$$T = \frac{-3n}{2\sqrt{m^3}}; \Delta = \left(\frac{q}{2}\right)^2 + \left(\frac{p}{3}\right)^3;$$

$$a_1 = -\left(\frac{M_\theta}{DI} + \frac{(E-D)Bt^2\sigma_s}{4IDE}\right); c_1 = \frac{(E-D)B\sigma_s^3}{3IDE^3};$$

$$p_1 = -\frac{a_1^2}{3}; q_1 = \frac{2a_1^3}{27} + c_1;$$

$$m_1 = -3p_1 \ (m_1 > 0); n_1 = -9q_1; \xi_1 = \arccos T_1;$$

$$T_1 = \frac{-3n_1}{2\sqrt{m_1^3}}; \Delta_1 = \left(\frac{q_1}{2}\right)^2 + \left(\frac{p_1}{3}\right)^3.$$

3.3 Discrete analysis

According to the above static analysis and elastic-plastic analysis, \bar{M}_a is an unknown variable, so the static bending of the roll bending

stage is an indeterminate problem. However, the relationship between the outer bending moment and bending curvature cannot be determined by using the existing static equilibrium conditions and the relationship between the inner bending moment and bending curvature. Therefore, it is necessary to seek other conditions.

By using the idea of geometric discretization, one-third of the circular pipe is uniformly divided into N equal parts along the circumference, in other words, one-third of the circular pipe is composed of N pipe-wall elements with the same geometric parameters and connected by nodes. As shown in Fig. 5, from the origin of the coordinate system, each element serial number is ①, ②, ③... , the node serial number is 0, 1, 2... N . Taking the node i ($i \leq N$) as the origin of coordinate, and taking the tangential direction and the normal direction of the geometric neutral layer of the pipe at the node i as the x_i axis and y_i axis, thus the local follow-up coordinate system is established.

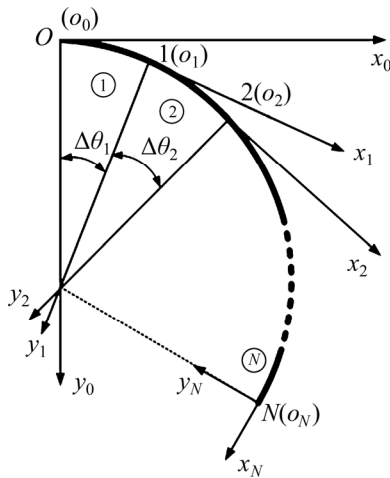


Fig. 5 One-third discrete circular pipe

As shown in Fig. 6, the pipe-wall element i is taken as the research object. Under the local coordinate system $x_{i-1}o_{i-1}y_{i-1}$, the coordinate $(x_{i0}^{i-1}, y_{i0}^{i-1})$ of the node i before loading can be represented as

$$\begin{cases} x_{i0}^{i-1} = R \sin(\Delta\theta_{i0}) \\ y_{i0}^{i-1} = R(1 - \cos(\Delta\theta_{i0})) \end{cases} \quad (17)$$

$$\Delta\theta_{i0} = \frac{2\pi}{3N} \quad (18)$$

where x_{i0}^{i-1} is the initial x -coordinate of the node i in the coordinate system $x_{i-1}o_{i-1}y_{i-1}$ (mm); y_{i0}^{i-1} is the initial y -coordinate of the node i in the

coordinate system $x_{i-1}o_{i-1}y_{i-1}$ (mm); $\Delta\theta_{i0}$ is the initial angle between the pipe-wall cross-section where the node i is located and the axis y_{i-1} (rad).

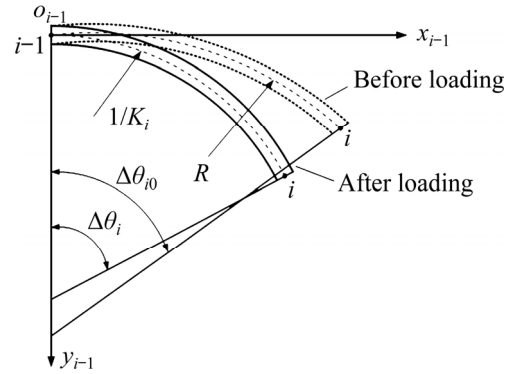


Fig. 6 Pipe-wall element before and after loading

After loading, the coordinate is (x_i^{i-1}, y_i^{i-1}) , which is expressed as

$$\begin{cases} x_i^{i-1} = \frac{1}{K_i} \sin(\Delta\theta_i) \\ y_i^{i-1} = \frac{1}{K_i} [1 - \cos(\Delta\theta_i)] \end{cases} \quad (19)$$

where x_i^{i-1} is the loaded x -coordinate of the node i in the coordinate system $x_{i-1}o_{i-1}y_{i-1}$ (mm); y_i^{i-1} is the loaded y -coordinate of the node i in the coordinate system $x_{i-1}o_{i-1}y_{i-1}$ (mm); K_i is the curvature of the pipe-wall element i after loading; $\Delta\theta_i$ is the angle between the pipe-wall cross-section where the node i is located and the axis y_{i-1} after loading (rad).

According to the basic assumption (1), the length of the pipe-wall element remains unchanged before and after deformation, the following can be obtained:

$$\frac{1}{K_i} \Delta\theta_i = R \Delta\theta_{i0} \quad (20)$$

In order to obtain the final contour curve of the deformed pipe-wall cross-section, the coordinates of each node should be unified according to the relationship among the local coordinate systems. Therefore, according to the definition of the local coordinate system, the coordinate value (x_i^i, y_i^i) is

$$\begin{cases} x_i^i = 0 \\ y_i^i = 0 \end{cases} \quad (21)$$

According to Eqs. (17)–(20), the coordinates of each node are unified into the local coordinate system $x_0o_0y_0$, and the iterative formula can be expressed as

$$\begin{cases} x_i^0 = x_{i-1}^0 + x_{i-1}^{i-1} \cos \theta_{i-1} - y_{i-1}^{i-1} \sin \theta_{i-1} \\ y_i^0 = y_{i-1}^0 + x_{i-1}^{i-1} \sin \theta_{i-1} + y_{i-1}^{i-1} \cos \theta_{i-1} \end{cases} \quad (22)$$

$$\theta_{i-1} = R\Delta\theta_0 \sum_1^{i-1} K_i \quad (23)$$

where θ_{i-1} is the angle between the pipe-wall cross-section where the node $i-1$ is located and the axis y_0 after loading (rad).

3.4 Solution of statically indeterminate problem

Because the static bending is a primary statically indeterminate problem, a compatibility equation of deformation is required to solve it. Depending on the continuity and symmetry of the bending deformation, the pipe-wall cross-section where the node 0 is located is always 120° from the y_N axis during the deformation process, and then,

$$\sum_{i=1}^N \Delta\theta_i = \frac{2}{3} \pi \quad (24)$$

By substituting Eqs. (18) and (20) into Eq. (24), the compatibility equation of deformation can be obtained as follows:

$$\sum_{i=1}^N K_i = \frac{N}{R} \quad (25)$$

When the deformation of the pipe is large enough, the outer-wall of the pipe will fit with the surface of each roller, so the pipe cross-section is divided into two regions: non-attaching-roller region and attaching-roller region. In the non-attaching-roller region, the curvature of the outer-wall of the pipe cannot be greater than the surface curvature of each roller, because the pipe-wall element is restrained by each roller. In the attaching-roller region, since the pipe-wall element and each roller have been fitted, the outer-wall curvature of the pipe is equal to the surface curvature of each roller. Thus, after loading, the curvature K_i of geometric neutral layer of the pipe needs to meet the following condition:

$$K_i \leq \frac{2}{2R_1 + t} \quad (26)$$

The load increment method is used to solve the relation among the loading force F of each roller, the bending curvature K , and reduction H . The loading force of each roller is evenly divided into several loading increments and applied step by step.

And in each increment step, parameters such as bending curvature and node coordinates of each element are solved iteratively. It is supposed that the loading increment of each step of each roller is f , and the number of loading increment steps is k . According to Eq. (7), the bending moment of the pipe-wall element i can be obtained as follows:

$$\bar{M}_{\theta_i}^k = \bar{M}_a + \frac{fk}{2} R \sin \theta_i - \frac{\sqrt{3}}{6} fkR(1 - \cos \theta_i) \quad (27)$$

$$\theta_i = \frac{2\pi i}{3N} \quad (28)$$

where $\bar{M}_{\theta_i}^k$ is the outer bending moment of the pipe-wall cross-section where the node i is located after loading k times (N·mm); θ_i is the angle between the pipe-wall cross-section where the node i is located and the axis y (rad).

Since the inner and outer bending moments of arbitrary cross-section of the pipe are equal in the deformation process, namely,

$$M_\theta = \bar{M}_{\theta_i} \quad (29)$$

Combined with Eqs. (16), (27), (28) and (29), the geometric neutral layer curvature of the pipe-wall element after loading can be obtained as follows:

$$K_i = \phi(\phi(M_a, F)) \quad (30)$$

where ϕ is the iteration error.

When the loading force of each roller is known, Eqs. (24), (25) and (30) constitute a system of nonlinear equations for $N+1$ elements about M_a and $K_i (i=1, 2, \dots, N)$ composed of $N+1$ equations. Furthermore, in each incremental step, Eqs. (24) and (25) are used as the discriminant conditions to carry out one-dimensional iterative search solution for M_a . The initial iteration value of M_a is set to zero, and λ is the iteration step, as shown in Fig. 7.

4 Numerical simulations

4.1 Finite element model

By using ABAQUS 6.10 software packages, the finite element model of three-roller continuous setting round process is established, as shown in Fig. 8. Then, two sets of pipes of different materials with the thickness of 2 mm are selected. The geometrical dimensions and material properties of pipes and rollers are shown in Tables 1 and 2. Since the main research object of the process is thin-walled metal pipes, the pipe is set to a deformable

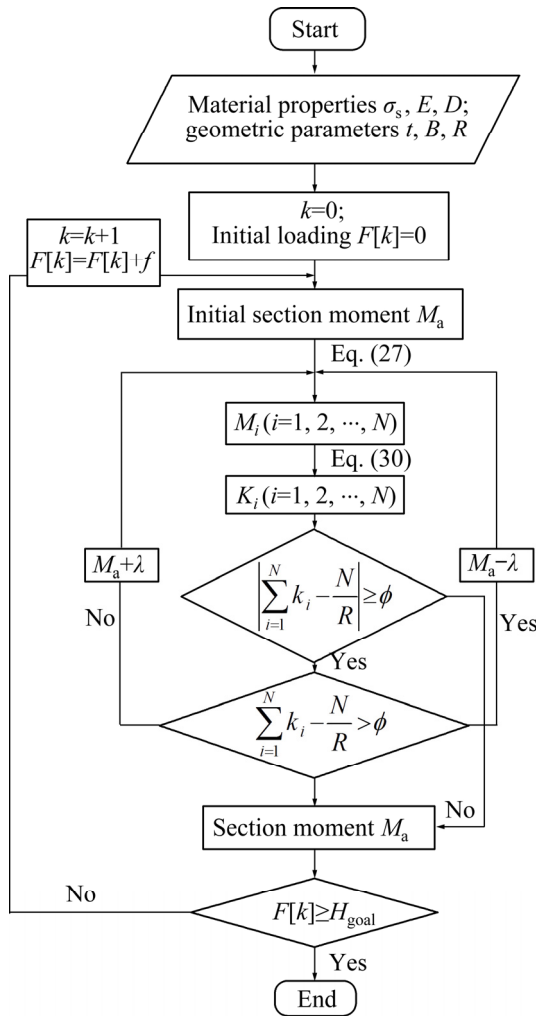


Fig. 7 Program flow of mechanical model

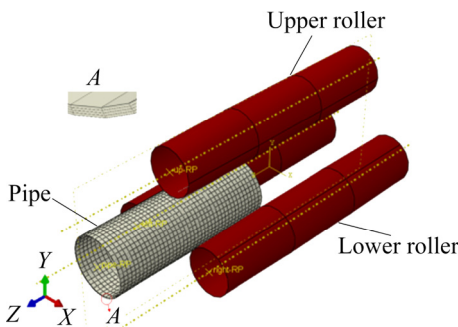


Fig. 8 Finite element model of three-roller continuous setting round process

body. Also considering the symmetry of the deformation condition, one-third of the pipe is modeled. And the pipe is discretized by using the 8-node linear hexagonal incompatible module elements (C3D8I). In addition, because the strength and stiffness of each roller are much greater than those of the pipe, it is set as analytical rigid. Finally, the contact property between the outer surface of

the pipe and the outer surface of each roller is defined as face-to-face contact. The sliding formula is finite sliding. The tangential property is a penalty function, and the friction coefficient is 0.18.

Table 1 Geometric dimensions of pipes and rollers

D_p /mm	L /mm	D_g /mm	α_j /rad	α_x /rad	L_g /mm
120, 140, 160	600	120	0.022	0.015	600

L —Length of pipe; D_g —Diameter of roller

Table 2 Material performance parameters of pipes

Material	E /GPa	σ_s /MPa	D /MPa
ST12	179	189	1500
304	234	294	2842

ST12— ST12 stainless steel; 304—304 stainless steel

4.2 Results and discussion

4.2.1 Deformation behavior

As can be seen from Fig. 9, there are six regions along the circumference of the pipe, namely three positive bending regions and three reverse bending regions, which are evenly distributed on the entire pipe cross-section.

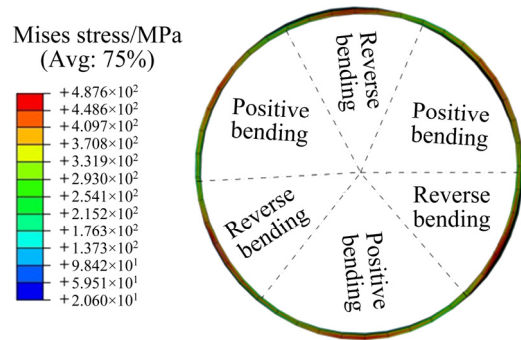


Fig. 9 Distribution of equivalent stress at roll bending stage (Material: 304, $t=2$ mm)

Similarly, it can be seen from Fig. 10 that the residual stress of each micro-section of the unloaded pipe is relatively small and varies between 8.4 and 60.3 MPa, and the distribution of the residual stress is relatively uniform. Additionally, the main reason for the residual stress in the pipe after unloading is that the deformation degrees of the inner and outer layers of the pipe are inconsistent during the reciprocating bending process. The residual stress is the key to judge the quality of pipes, that is, the smaller the residual stress is, the better the quality of a pipe is.

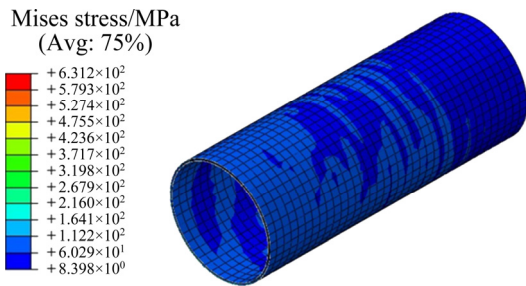


Fig. 10 Distribution of equivalent stress in unloading stage (Material: 304, $t=2$ mm)

The equivalent stress of 5 nodes along the thickness direction of the pipe is extracted at the two stages of roll bending and unloading, as can be seen from Fig. 11. During the roll bending stage, the equivalent stress gradually decreases from the inner layer (Node 1) and outer layer (Node 5) to the geometric neutral layer (Node 3) of the pipe, and the equivalent stress is symmetrically distributed about the geometric neutral layer. During the unloading stage, the equivalent stress of the pipe inner and outer layers decreases significantly and is slightly different from that of the geometric neutral layer, indicating that there is no stress concentration and the residual stress of the pipe is very small after unloading.

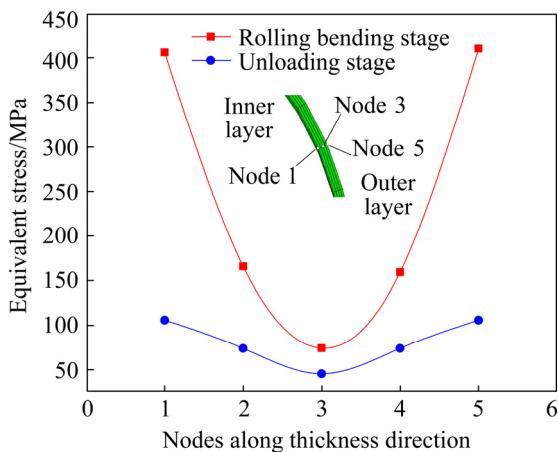


Fig. 11 Distribution of equivalent stress along thickness direction (Material: 304, $t=2$ mm)

The equivalent stress of outer circumferential nodes of the pipe is extracted at the two stages of roll bending and unloading, as shown in Fig. 12. During the roll bending stage, the equivalent stress of the pipe shows a waveform distribution along the circumferential direction with six peaks corresponding to each bending region. The

equivalent stress decreases from the center of each bending region to both sides of the pipe. Since the contact between the pipe and the roller is linear, the reverse bending region is smaller than the positive bending region. Furthermore, after the pipe is unloaded, the loading force of each roller on the pipe is gradually reduced, and the equivalent stress of each node of the pipe tends to be similar and fluctuates about 50 MPa.

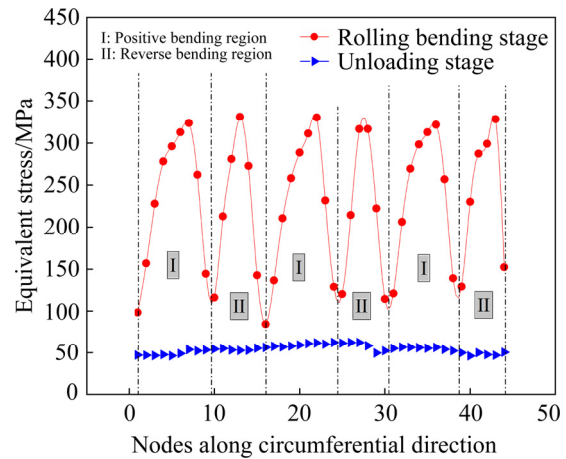


Fig. 12 Distribution of equivalent stress along circumferential direction (Material: 304, $t=2$ mm)

The distribution of the maximum and minimum principal stresses at the roll bending stage is shown in Fig. 13, and the results are shown in Table 3. Positions *A* and *C* are located in the reverse bending region, and the maximum principal stress is generated in the inner layer of the pipe (Nodes 2494 and 3076), while the minimum principal stress is generated in the outer layer of the pipe (Nodes 3313 and 3895), respectively. Position *B* is in the positive bending region, and the maximum and minimum principal stresses are generated in the outer layer of the pipe (Node 3576) and the inner layer of the pipe (Node 2757), respectively. Therefore, the absolute values of the maximum and minimum principal stresses at each position of the pipe are basically equal, proving that the deformation characteristics of the pipe are consistent with the pure bending characteristics.

Figure 14 shows the change of loading force of each roller with time. This process has a total of 600 s. 0–200 s is the loading stage, when $t=75$ s, three rollers start to contact with the pipe, and the loading force of each roller increases gradually. 200–400 s is the roll bending stage, during 250–350 s, the loading force of each roller

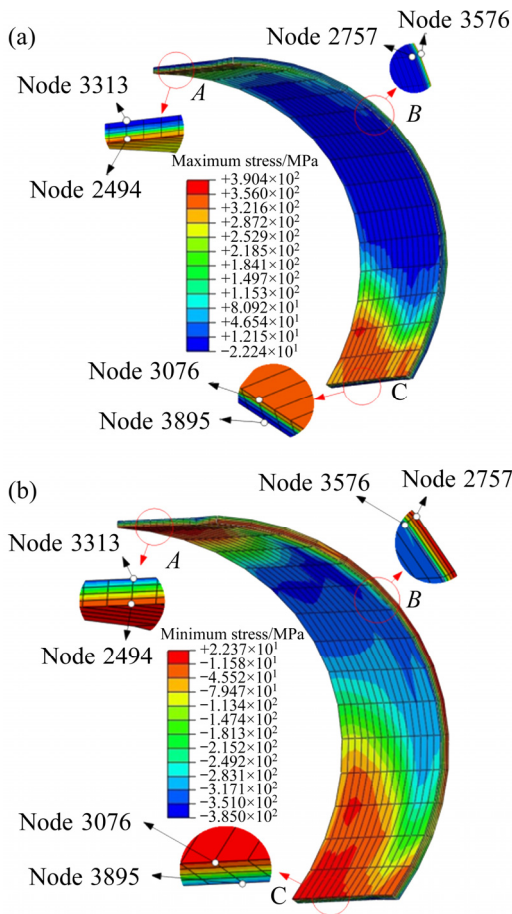


Fig. 13 Distribution of maximum (a) and minimum (b) principal stresses (Material: 304, $t=2$ mm)

Table 3 Maximum and minimum principle stresses

Position	Node ID	Principle stress/MPa	
		Maximum	Minimum
A	2494	+331	–
	3313	–	–332
B	3576	+343	–
	2757	–	–349
C	3076	+330	–
	3895	–	–333

reaches the maximum value and shows a stable trend. 400–600 s is the unloading stage, the loading force of each roller gradually decreases, and when $t=525$ s, the roller begins to separate from the pipe. In a word, the loading force of each roller increases, stabilizes and decreases with time. At the same time, the absolute value of the loading force of three rollers is basically the same, proving that the loading forces of three rollers are equal in the continuous setting round process.

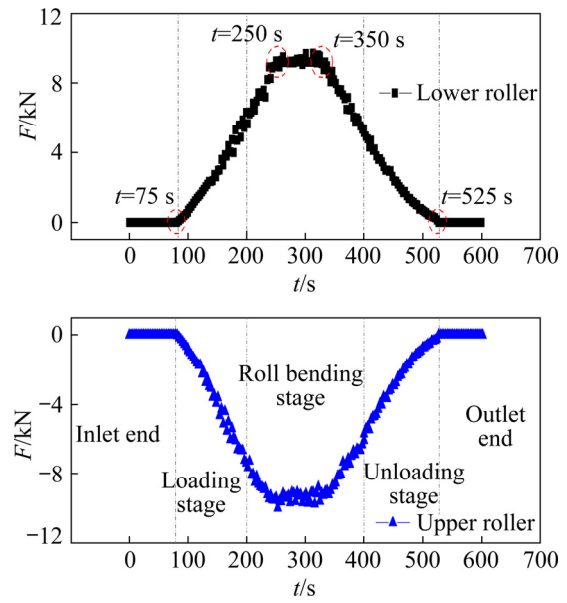


Fig. 14 Variation of loading force of each roller with time (Material: 304, $t=2$ mm)

4.2.2 Comparison of theoretical and simulation results

Built on the above theoretical model and finite element model, it is assumed that one-third of the circular pipe is composed of 1000 micro-pipe-wall elements, namely, $N=1000$. Then through theoretical analysis and numerical simulation, the calculation results of the horizontal cross-section force, bending moment, bending curvature and loading force of each roller are obtained.

Figure 15 shows the relationship between horizontal cross-section force and bending moment in the theoretical analysis. It can be seen from Fig. 15 that, for different pipe-wall thicknesses, the horizontal cross-section forces F_a and F_b increase with the increase of the reduction H , and the turning point of two curves is the elastic–plastic demarcation point. Additionally, the bending moments M_a and M_b gradually increase with the increase of H , and gradually approach to the constant value, which indicates the beginning of the roll bending stage. The greater the thickness of the pipe, the greater the horizontal cross-section force and bending moment.

Figure 16 shows the distribution of bending curvature and bending moment obtained by theoretical calculation along the one-third circular pipe. The result shows that the whole pipe has three positive bending regions and three reverse bending regions, which is consistent with the simulation

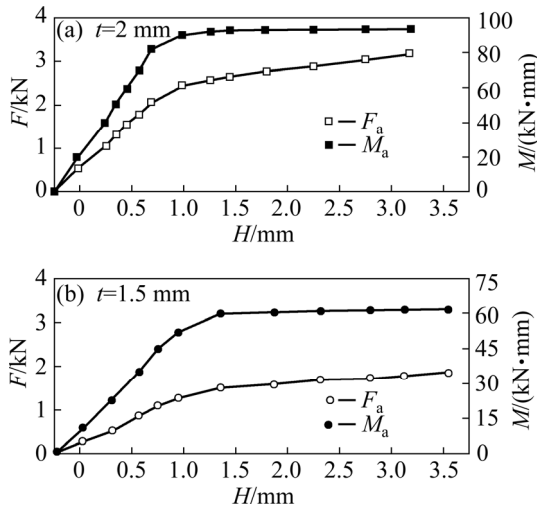


Fig. 15 Variation of horizontal cross-section force and bending moment with reduction (Material: 304; $F_a=F_b$, $M_a=M_b$)

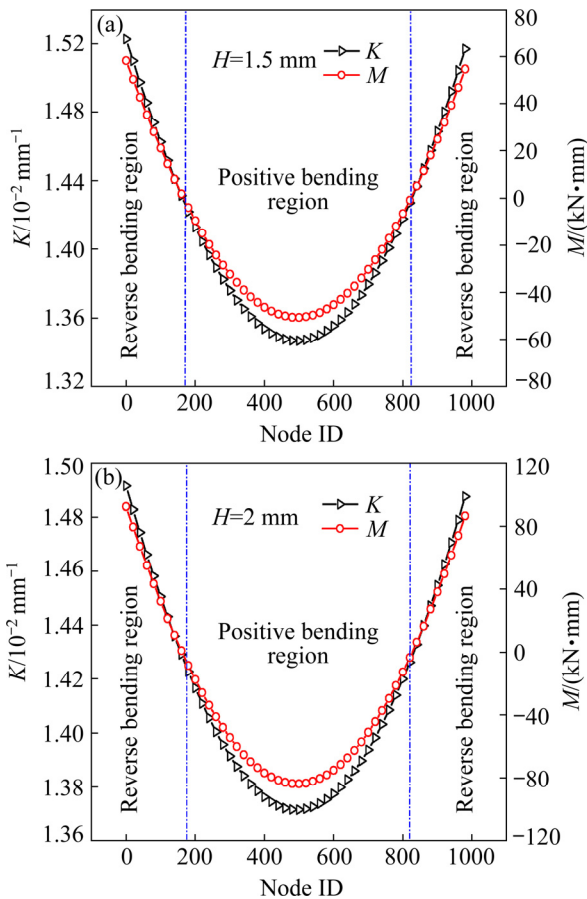


Fig. 16 Distribution of bending curvature and bending moment of one-third pipe (Material: 304)

results of Fig. 9. As can be seen from Fig. 16, for different thicknesses, when $K > 1/R$ and $M > 0$, the region where the pipe is located is the reverse bending region. On the contrary, when $K < 1/R$ and $M < 0$, the region where the pipe is located is the

positive bending region. Furthermore, the maximum bending curvature K_{\max} appears in the center of the pipe in contact with the roller, and the minimum bending curvature K_{\min} appears in the center of the region between any two rollers.

The changes of the maximum bending curvature K_{\max} and minimum bending curvature K_{\min} with the reduction H are shown in Fig. 17. As can be observed in Fig. 17, at the beginning, the maximum bending curvature of the pipe increases linearly with the increase of the reduction. When the maximum bending curvature increases to the position of the elastic–plastic demarcation point, the outer-wall of the pipe begins to contact with the roller until the maximum bending curvature of the pipe increases slowly and gradually becomes stable. The minimum bending curvature decreases with the increase of the reduction. In addition, the decrease speed of the minimum bending curvature is almost equal to the increase speed of the maximum bending curvature, which proves that the plastic deformation occurs simultaneously in the positive and reverse bending regions.

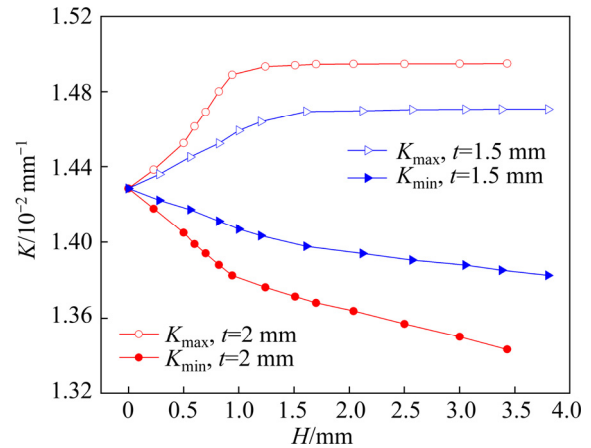


Fig. 17 Variation of maximum and minimum bending curvatures with reduction (Material: 304)

Figure 18 shows the loading outline of one-third pipe obtained by theoretical calculation and numerical simulation. According to the curvature distribution of the loaded pipe as shown in Fig. 18, there are three positive bending regions and three reverse bending regions in the whole pipe cross-section. The theoretical fitting curve outline is in good agreement with that of the simulated curve outline after unloading.

Figure 19 shows the relationship between the loading force of each roller and the reduction

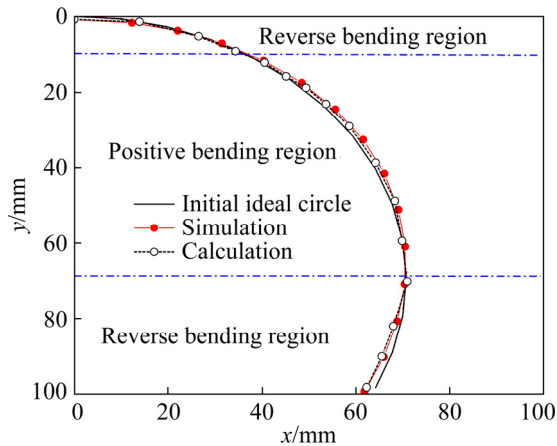


Fig. 18 Outline of one-third pipe after loading (Material: 304, $t=2$ mm)

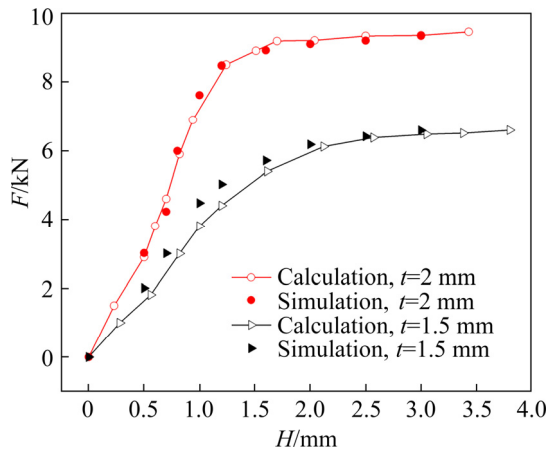


Fig. 19 Relationship between loading force of each roller and reduction (Material: 304, $t=2$ mm)

obtained by theoretical calculation and numerical simulation. As can be seen from Fig. 19, the loading force of each roller increases with the increase of the reduction. The pipes with the thickness of 2 and 1.5 mm begin to produce plastic deformation under the reduction of 1.5 and 2.0 mm respectively, indicating that the reduction required for plastic deformation decreases with the increase of pipe-wall thickness. The error between the theoretical fitting curve and the simulated data point is very small, which indicates that the simulation results verify the reliability of the theoretical calculation.

5 Experimental

5.1 Materials

ST12 and 304 stainless steel plates are made by rolling machine with the thickness of 2 and

1.5 mm and outer diameter of 140 and 160 mm, respectively. Then each pipe is pressed to form an oval. The pipe with different initial ovalities can be obtained by changing the pressure.

5.2 Experimental process

Firstly, under the preset process parameters, the pipe is placed on the setting round equipment, and the cylinder supports the balance of the pipe to be setting round. Then, the actuating motor is controlled by the numerical control system to drive the lower rollers to rotate at a constant speed synchronously, so as to ensure the rotation of the pipe in the process of continuous setting round. Meanwhile, the upper roller also starts to rotate under the action of the friction force of the pipe. At the same time, the actuating motor (located inside of the equipment pedestal) on the linear sliding platform module is controlled to ensure that the pipe can advance at a uniform speed under the action of the push plate, so as to complete the whole continuous setting round process. The experimental equipment is shown in Fig. 20.

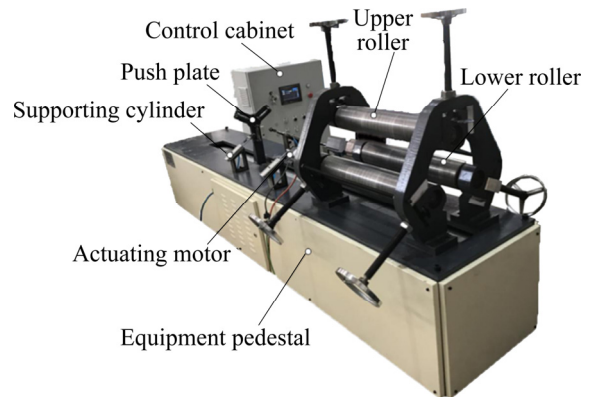


Fig. 20 Experimental equipment

The coordinates of points around the outer diameter of the pipe after unloading are obtained by using CMM, and the lattice data are imported into UG software for fitting. By substituting the data of the long axis and short axis of the pipe into Eq. (31), the residual ovality (δ) of the pipe can be calculated.

$$\delta = \frac{2(a-b)}{D_p} \times 100\% \tag{31}$$

where a is the long axis radius of the pipe (mm); b is the short axis radius of the pipe (mm).

5.3 Results and discussion

It can be seen from Fig. 21 that the residual ovality of the pipe gradually decreases with the increase of the reduction. Moreover, the reduction when the decreasing trend of residual ovality begins to flatten is selected as the optimum reduction of the pipe. That is, for ST12 pipes and 304 pipes with an outer diameter of 140 mm and a thickness of 2 mm, the optimum reductions are 1.5 and 2.0 mm, respectively (δ_0 is the initial ovality).

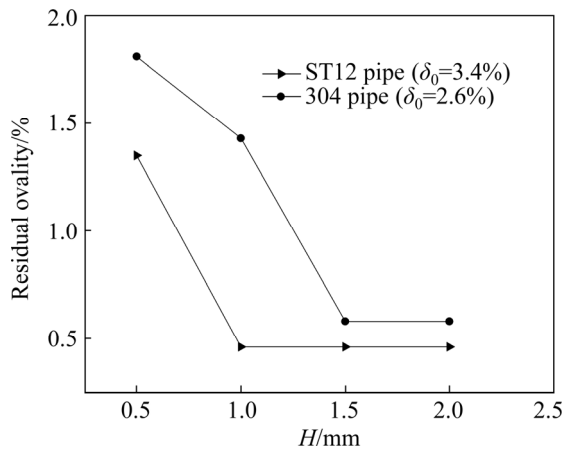


Fig. 21 Effect of reduction on residual ovality

Figure 22 shows the change of the residual ovality of 304 pipes with different initial ovalities under the optimum reduction. According to Fig. 22, under the optimum reduction, the difference between the residual ovality of the pipes with different initial ovalities is very small, indicating that the residual ovality is independent of the initial ovality. This result effectively proves that the reciprocating bending can eliminate the difference of the initial curvature and finally unify the curvature to the same direction and value [16].

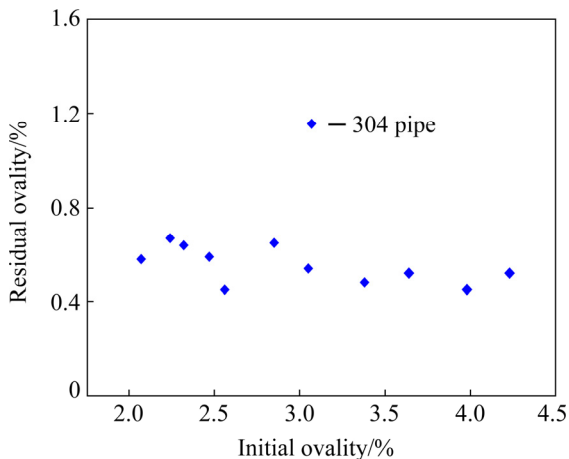


Fig. 22 Effect of initial ovality on residual ovality

The relative thickness of the pipe is defined as t/D_p . Figure 23 shows that the optimum reduction of the pipe decreases with t/D_p . And corresponding to the same relative thickness, the optimum reduction of 304 pipes is larger than that of ST12 pipes. In addition, Fig. 24 shows the forming effect of pipes after springback.

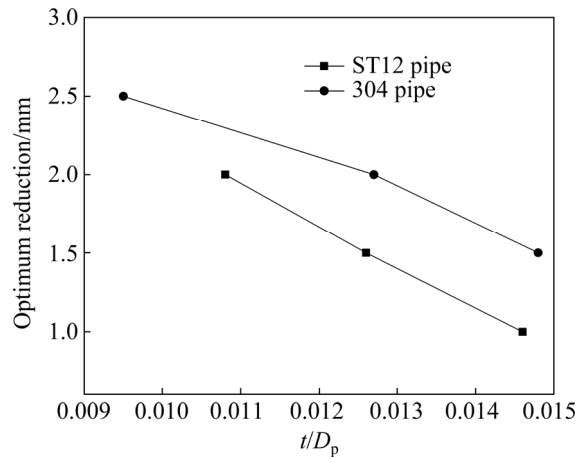


Fig. 23 Effect of relative thickness on optimum reduction

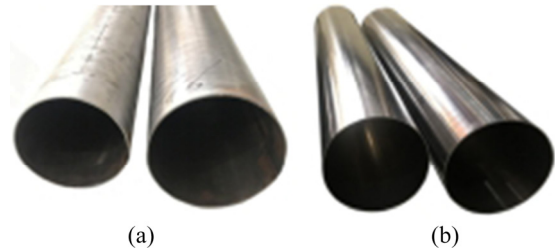


Fig. 24 Forming effect of ST12 (a) and 304 (b) pipes

6 Conclusions

(1) The three-roller continuous setting round process for LSAW pipes is proposed firstly, which can be divided into three stages: loading stage, roll bending stage and unloading stage. It is especially suitable for thin-walled metal pipes with large length to diameter ratio and small thickness to diameter ratio.

(2) During the process, there are three positive bending regions and three reverse bending regions along the circumference of the pipe. The loading force of each roller shows an increasing, stable and decreasing trend with time.

(3) The error between the theoretical fitting curve and the simulated data point is very small, and the simulation results verify the reliability of the theoretical calculation. The residual ovality of the pipes decreases with the increase of the

reduction, and the reduction of the turning point is the optimum reduction. The experimental results show that the ovality of pipes can be less than 0.7% without cross-section distortion, which verifies the feasibility of three-roller continuous setting round process.

Acknowledgments

This work is supported by the National Natural Science Foundation of China (Nos. 52005431, 51705449 and 51975509), the Natural Science Foundation of Hebei Province of China (No. E2020203086), and the National Major Science and Technology Projects of China (No. 2018-ZX04007002).

Appendix

According to Cardano formula and Shengjin formula, the roots of Eq. (14) is determined, and the process is as follows:

(1) Positive bending elastic-plastic deformation

$$\Delta K^3 - \Delta K^2 \left(\frac{M_\theta}{DI} + \frac{(D-E)Bt^2\sigma_s}{4IDE} \right) + \frac{(D-E)B\sigma_s^3}{3IDE^3} = 0 \tag{A1}$$

For the general cubic equation of a single variable: $y^3+ay^2+by+c=0$. Set $y=x-a/3$, then the form of $x^3+px+q=0$ can be deduced. Therefore, according to Eq. (A1), it can be obtained that

$$y^3 + ay^2 + c = 0 \tag{A2}$$

Then, by substituting $y=x-a/3$ into Eq. (A2), we can get

$$x^3 - \frac{a^2}{3}x + \frac{2a^3}{27} + c = 0 \tag{A3}$$

When $\Delta = (\frac{q}{2})^2 + (\frac{p}{3})^3 \geq 0$, the rational number root can be obtained:

$$K_\theta = \sqrt[3]{-\frac{q}{2} + \sqrt{(\frac{q}{2})^2 + (\frac{p}{3})^3}} + \sqrt[3]{-\frac{q}{2} - \sqrt{(\frac{q}{2})^2 + (\frac{p}{3})^3}} - \frac{a}{3} + K_0 \tag{A4}$$

When $\Delta = (\frac{q}{2})^2 + (\frac{p}{3})^3 < 0$, the positive integer roots are required, then,

$$K_\theta = \frac{2 \cos(\frac{\xi - \pi}{3}) \sqrt{m}}{3} - \frac{a}{3} + K_0 \tag{A5}$$

(2) Elastic deformation

$$K_\theta = \frac{M_\theta}{EI} + K_0 \tag{A6}$$

(3) Reverse bending elastic-plastic deformation

$$\Delta K^3 - \Delta K^2 \left(\frac{M_\theta}{DI} + \frac{(E-D)Bt^2\sigma_s}{4IDE} \right) + \frac{(E-D)B\sigma_s^3}{3IDE^3} = 0 \tag{A7}$$

Similarly, we can get

$$y^3 + a_1y^2 + c_1 = 0 \tag{A8}$$

Then, by substituting $y = x - \frac{a_1}{3}$ into Eq. (A8), we can get

$$x^3 - \frac{a_1^2}{3}x + \frac{2a_1^3}{27} + c_1 = 0 \tag{A9}$$

When $\Delta_1 = (\frac{q_1}{2})^2 + (\frac{p_1}{3})^3 \geq 0$, the rational number root can be obtained:

$$K_\theta = \sqrt[3]{-\frac{q_1}{2} + \sqrt{(\frac{q_1}{2})^2 + (\frac{p_1}{3})^3}} + \sqrt[3]{-\frac{q_1}{2} - \sqrt{(\frac{q_1}{2})^2 + (\frac{p_1}{3})^3}} - \frac{a_1}{3} + K_0 \tag{A10}$$

When $\Delta_1 = (\frac{q_1}{2})^2 + (\frac{p_1}{3})^3 < 0$, and positive integer roots are required, then,

$$K_\theta = \frac{2 \cos(\frac{\xi_1 - \pi}{3}) \sqrt{m_1}}{3} - \frac{a_1}{3} + K_0 \tag{A11}$$

References

[1] JUNIOR R L, JUNIOR M M W, SOUZA V B D, REIS J, MATTOS H S D C. Plastic collapse of thin-walled elastoplastic pipes under internal pressure and superposed axial loading [J]. International Journal of Pressure Vessels and Piping, 2020, 180: 104043.
 [2] HOSSEINI A, RAHMATABADI D, HASHEMI R, AKBARI H. Experimental and numerical assessment of energy

- absorption capacity of thin-walled Al 5083 tube produced by PTCAP process [J]. Transactions of Nonferrous Metals Society of China, 2020, 30(5): 1238–1248.
- [3] CHEGENI B, JAYASURIYA S, DAS S. Effect of corrosion on thin-walled pipes under combined internal pressure and bending [J]. Thin-Walled Structures, 2019, 143: 106218.
- [4] ZHAO Xiao-xin, XU Lian-yong, JING Hong-yang, HAN Yong-dian, ZHAO Lei, CAO Jun, LV Yi, SONG Zheng-rong. A strain-controlled fracture assessment for submarine thin-walled pipes with V-groove welds and circumferential embedded cracks [J]. Thin-Walled Structures, 2019, 145: 106377.
- [5] BAYKASOĞLU A, BAYKASOĞLU C, CETIN E. Multi-objective crashworthiness optimization of lattice structure filled thin-walled tubes [J]. Thin-Walled Structures, 2020, 149: 106630.
- [6] HUANG Zhi-Xin, ZHANG Xiong. Three-point bending of thin-walled rectangular section tubes with indentation mode [J]. Thin-Walled Structures, 2019, 137: 231–250.
- [7] JIANG Lan-fang, ZHANG Shu-you, WANG Ya-qun, FENG Yi-xiong, LIN Yao-chen, LIU Hong, ZHANG Fei, SHAO Hong. Research on bending forming method of large diameter-thickness ratio thin-walled tubes for aerospace [J]. The International Journal of Advanced Manufacturing Technology, 2019, 102: 3037–3049.
- [8] TAO Zhi-jun, FAN Xiao-guang, YANG He, MA Jun, LI Heng. A modified Johnson–Cook model for NC warm bending of large diameter thin-walled Ti–6Al–4V tube in wide ranges of strain rates and temperatures [J]. Transactions of Nonferrous Metals Society of China, 2018, 28(2): 298–308.
- [9] YU Gao-chao, ZHAO Jun, ZHAO Fei-ping. Elastic-plastic secondary indeterminate problem for thin-walled pipe through the inner-wall loading by three-point bending [J]. Mechanics Based Design of Structures and Machines, 2017, 45(2): 219–238.
- [10] LI Heng, XU Jie, YANG Heng, YANG He, LI Guang-jun. Sequential multi-objective optimization of thin-walled aluminum alloy tube bending under various uncertainties [J]. Transactions of Nonferrous Metals Society of China, 2017, 27(3): 608–615.
- [11] ZHAO Jun, YIN Jing, MA Rui, MA Li-xia. Springback equation of small curvature plane bending [J]. Scientia Sinica Technologica, 2011, 054(009): 2386–2396.
- [12] ZHAO Jun, CAO Hong-qiang, ZHAN Pei-pei, MA Rui. Pure bending equivalent principle for over-bend straightening and its experimental verification [J]. Journal of Mechanical Engineering, 2012, 48(8): 28–33. (in Chinese)
- [13] ZHAO Jun, ZHAN Pei-pei, MA Rui, ZHAI Rui-xue. Control strategy of over-bending setting round for pipe-end of large pipes by mould press type method [J]. Transactions of Nonferrous Metals Society of China, 2012, 22(S2): 329–334.
- [14] ZHAN Pei-pei, ZHAO Jun, SHANG Jing-hua, MA Rui. Study on control policy of over-bending setting round for pipe ends of large pipes [J]. China Mechanical Engineering, 2013, 24(9): 1220–1224. (in Chinese)
- [15] ZHAN Pei-pei, ZHAO Jun, LI Ping, SHANG Jing-hua. Three steps control strategy of over-bending setting round for pipe-end of large pipes [J]. Materials Science and Technology, 2014, 22(2): 97–103. (in Chinese)
- [16] YU Gao-chao, ZHAO Jun, MA Rui, ZHAI Rui-xue. Uniform curvature theorem by reciprocating bending and its experimental verification [J]. Journal of Mechanical Engineering, 2016, 52(18): 57–63. (in Chinese)
- [17] YU Gao-chao, ZHAO Jun, XING Jiao-jiao, ZHAO Fei-ping, LI Sen-lin. Research on the symmetrical three-roller setting round process [J]. Journal of Mechanical Engineering, 2017, 053(014): 136–143. (in Chinese)
- [18] ZHAO Jun, YU Gao-chao, MA Rui. A mechanical model of symmetrical three-roller setting round process: The static bending stage [J]. Journal of Materials Processing Technology, 2016, 231: 501–512.
- [19] YU Gao-chao, ZHAO Jun, ZHAI Rui-xue, MA Rui, WANG Chun-ge. Theoretical analysis and experimental investigations on the symmetrical three-roller setting round process [J]. The International Journal of Advanced Manufacturing Technology, 2018, 94(1–4): 45–56.
- [20] HUANG Xue-ying, YU Gao-chao, ZHAO Jun, MU Zhen-kai, ZHANG Zhi-yuan, MA Rui. Numerical simulation and experimental investigations on a three-roller setting round process for thin-walled pipes [J]. The International Journal of Advanced Manufacturing Technology, 2020, 107: 355–369.
- [21] CAO Wen-ao, DING Hua-feng. A method for solving all joint reactions of 3R2T parallel mechanisms with complicated structures and multiple redundant constraints [J]. Mechanism and Machine Theory, 2018, 121: 718–730.
- [22] NAYAK P, SAHA K N. Analysis of statically indeterminate non-uniform bar problem in post elastic domain by an iterative variational method [J]. Applied Mathematical Modelling, 2017, 51: 86–108.
- [23] GHUKU S, SAHA K N. A semi-analytical solution of statically indeterminate bar problem by using domain decomposition method [J]. Perspectives in Science, 2016, 8: 661–663.
- [24] TAN Zou-qing, JIANG Xue-dong, HE Yun-song, XU Ran, XI Ren-qiang, BAN Shu-hao. Generalized variational principles for solutions of statically indeterminate trusses under mechanical-thermal-assembly loadings [J]. Journal of Engineering Mechanics, 2018, 144(1): 04017145.
- [25] LÓPEZ AM, SOSA P F M, SENACH J L B, PRADA M Á F. Influence of the plastic hinge rotations on shear strength in continuous reinforced concrete beams with shear reinforcement [J]. Engineering Structures, 2020, 207: 141–296.

大型直缝焊管三辊连续矫圆工艺

黄学颖^{1,2}, 赵军^{1,2}, 于高潮^{1,2}, 孟庆党^{1,2}, 穆振凯^{1,2}, 翟瑞雪^{1,2}

1. 燕山大学 先进锻压成形技术与科学教育部重点实验室, 秦皇岛 066004;
2. 燕山大学 机械工程学院, 秦皇岛 066004

摘要: 针对大型直缝焊管成形后存在的椭圆度过大和截面畸变等问题, 提出一种新的三辊连续矫圆工艺。该工艺可分为三个阶段: 加载阶段、辊弯矫圆阶段和卸载阶段。基于离散化的思想, 建立大型直缝焊管辊弯矫圆阶段的一次静不定问题的力学模型, 得到矫圆过程中管材的变形响应。模拟和理论计算结果表明, 管材截面沿周向存在三个正向弯曲区域和三个反向弯曲区域; 各辊载荷随时间呈现增长、稳定、下降趋势; 理论拟合曲线与模拟数据点之间的误差很小, 仿真结果验证了理论计算的可靠性。实验结果表明, 管材的残余椭圆度随压下量的增加而减小, 并且转折点处的压下量是管材的最佳压下量; 此外, 管材的残余椭圆度小于 0.7%, 且无截面畸变, 验证了大型直缝焊管三辊连续矫圆工艺的可行性。

关键词: 大型直缝焊管; 三辊连续矫圆; 静不定问题; 力学模型; 椭圆度; 最优压下量

(Edited by Xiang-qun LI)